Composition Variation Reveals the Non-Ideal Mixing of Components in $(Mg_{0.2}Co_{0.2}Ni_{0.2}Cu_{0.2}Zn_{0.2})O$ and the Benefits of this Variation in Sodium Ion-Battery

Modeste N. Tegomoh[1], Kug-Seung Lee[2], and Anne C. Co[1]

[1]Department of Chemistry and Biochemistry, The Ohio State University, Columbus, OH 43210, USA

[2]Pohang Accelerator Laboratory, POSTECH, Pohang 37673, Republic of Korea

The reversible transformation between a multiphase and single-phase state has been used as a hallmark for entropy stabilization in the system $(Mg_{0.2}Co_{0.2}Ni_{0.2}Cu_{0.2}Zn_{0.2})O$. it was shown that cations are fully random and homogeneous in this single-phase material, providing a way to estimate its configurational entropy. The deliberate variation of this entropy led to the conclusion that $(Mg_{0.2}Co_{0.2}Ni_{0.2}Cu_{0.2}Zn_{0.2})O$ is primarily stabilized by this configurational entropy. Here, we show that this phase transformation observed in $(Mg_{0.2}Co_{0.2}Ni_{0.2}Cu_{0.2}Zn_{0.2})O$ could originate from a Jahn-Teller distortion rather than entropy stabilization. We further demonstrate through composition variation that the consolute temperature depends on the nature of the components rather than the number of components. In addition, we show that there is significant cation ordering in these systems, further casting doubts on the role of configurational entropy as the main stabilizing term. Finally, we demonstrate that this compositional variation can be used to tune the voltage of these complex metal oxides to improve their reactivity in a sodium-ion cell.

I.

The concept of “high entropy alloys” (HEA) has generated considerable excitement in the materials community over the past several years[1-3]. HEA is loosely defined as a multi-component alloy with a minimum of five components in an equimolar amount with a calculated configurational entropy of 1.609R or more[1-3]. “R” here is the ideal gas constant. To be more accurate, entropy stabilization is observed when the enthalpy of formation (ΔH_f) is positive, and the entropy of formation (ΔS_f) is large enough to make the Gibbs free energy of formation (ΔG_f) negative at a given temperature. The formed material may thus be said to be entropy stabilized at the consolute temperature and may become unstable below this temperature. This concept has been expanded to the realm of complex ceramics[4] and oxides[5-8].

The first multi-component oxide system claimed to be stabilized by configurational entropy was first published in 2015 by Rost *et al*. [ref.[9]]. They claim to demonstrate unambiguously that configurational entropy is the primary stabilizing term in forming the

complex single-phase rock salt $(Mg_{0.2}Co_{0.2}Ni_{0.2}Cu_{0.2}Zn_{0.2})O$ material. Starting from the MgO, CoO, NiO, CuO, and ZnO binary metal mix, they showed the formation of the single-phase $(Mg_{0.2}Co_{0.2}Ni_{0.2}Cu_{0.2}Zn_{0.2})O$ compound at about 900 ^oC. As dictated by the equation $\Delta G = \Delta H + T\Delta S$, they showed that the single-phase $(Mg_{0.2}Co_{0.2}Ni_{0.2}Cu_{0.2}Zn_{0.2})O$ material undergoes a phase transition to a multiphase system at low temperature (750 ^oC) and back to a single phase at higher annealing temperature. The claim was that this simple phase transition experiment demonstrated that the single-phase material was stabilized by entropy. However, the idea of entropy stabilization in metal oxide systems is not a new concept. Entropy stabilized two component oxide systems with positive enthalpies of formation have been confirmed by calorimetry. They include certain spinels[10-13] such as $CuAl_2O_4$, $CuCr_2O_4$, CuF_2O_4, $CuGa_2O_4$, and $CuMn_2O_4$. Furthermore, Rost *et al*.[ref.[9]] claim through the use of extended X-ray absorption fine structure (EXAFS) that the cations are randomly distributed in the single-phase rock salt $(Mg_{0.2}Co_{0.2}Ni_{0.2}Cu_{0.2}Zn_{0.2})O$ material at low temperature after quenching. This allowed them to assume that the mixing of the binary metal oxides to form the single-phase material is ideal. They then calculated the configurational entropy of the single-phase material to be 1.61R using equation S1 of the supplementary information, allowing them to classify the material as “high entropy”, borrowing from the field of HEA. The quaternary metal oxides $(Co_{0.25}Ni_{0.25}Cu_{0.25}Zn_{0.25})O$, $(Mg_{0.25}Ni_{0.25}Cu_{0.25}Zn_{0.25})O$, $(Mg_{0.25}Co_{0.25}Cu_{0.25}Zn_{0.25})O$, $(Mg_{0.25}Co_{0.25}Ni_{0.25}Zn_{0.25})O$, $(Mg_{0.25}Co_{0.25}Ni_{0.25}Cu_{0.25})O$ that could be prepared by omitting a corresponding binary metal component from $(Mg_{0.2}Co_{0.2}Ni_{0.2}Cu_{0.2}Zn_{0.2})O$ all have the same configurational entropy of 1.39R, which is lower than 1.61R and were therefore classified as “medium entropy”. Rost *et al*. [ref.[9]] claim that these “medium entropy” compounds could not transition from a multi-component mixture to a single-phase material at the same temperature as the “high entropy” counterpart. Their rationale was that these quaternary oxide system consolute temperatures are higher since they have lower configurational entropy. These observations led them to conclude that $(Mg_{0.2}Co_{0.2}Ni_{0.2}Cu_{0.2}Zn_{0.2})O$ was stabilized to a single-phase by the configurational entropy.

Since Sakar *et al*.[ref.[7]] demonstrated that micrometer-size particles of the “high entropy” oxide $(Mg_{0.2}Co_{0.2}Ni_{0.2}Cu_{0.2}Zn_{0.2})O$ show outstanding electrochemical performance in lithium-ion battery application, several related structures have been investigated, such as the spinel $(Co_{0.2}Mn_{0.2}V_{0.2}Fe_{0.2}Zn_{0.2})_3O_4$[ref.[14]], $(Mg_{0.2}Cr_{0.2}Mn_{0.2}Fe_{0.2}Co_{0.2})O$ (ref.[15]), $(Cr_{0.2}Mn_{0.2}Fe_{0.2}Co_{0.2}Ni_{0.2})O$ (ref.[15]), $(FeCoNiCrMnXLi)_3O_4$ (X = Cu, Mg, Zn) (ref.[16]), $(TiFeCoNiZn)_3O_4$ (ref.[17]), and $(Mg_{0.2}Ti_{0.2}Zn_{0.2}Cu_{0.2}Fe_{0.2})O$ (ref.[18]) with similar electrochemical performance. However, to our knowledge, no one has reported a successful application of these complex oxides as anode material for sodium ion application. Sodium-ion batteries have been considered a good alternative to lithium-ion batteries, particularly in large-scale energy storage, due to the abundance and low cost of sodium sources[19-21]. Ghigna *et al*.[ref.[22]] reported that $(Mg_{0.2}Co_{0.2}Ni_{0.2}Cu_{0.2}Zn_{0.2})O$ is inactive as an anode material in sodium-ion battery applications. To explain their findings, they investigated the lithium storage mechanism in this compound. They suggested it involves the formation (during lithiation) and removal

(during delithiation) of Li_xZn and Li_xMg intermetallic phases after the reduction of the parent oxide in the first discharge cycle. Since sodium does not form any intermetallic phases with Zn and Mg, they concluded it was the primary reason for the inactivity.

In the first part of this work, we show that the quaternary metal oxides $(Co_{0.25}Ni_{0.25}Cu_{0.25}Zn_{0.25})O$, $(Mg_{0.25}Ni_{0.25}Cu_{0.25}Zn_{0.25})O$, $(Mg_{0.25}Co_{0.25}Cu_{0.25}Zn_{0.25})O$, $(Mg_{0.25}Co_{0.25}Ni_{0.25}Zn_{0.25})O$, $(Mg_{0.25}Co_{0.25}Ni_{0.25}Cu_{0.25})O$ with "medium entropy" have transition temperature that depends on the nature of components rather than the number of components. This throws significant doubt on configurational entropy as the primary stabilizing term. We also show that the phase transition observed during the temperature cycle (high and low temperature phase change) may be due to the strain introduced in these systems by the Jahn-Teller distortion initiated by the Cu^{2+} in the octahedral environment. This suggests that only with sufficient thermodynamic characterization to show that the entropy of formation dominates over the enthalpy of formation can an oxide be rigorously classified as a high entropy oxide. In addition, we show that significant cation ordering occurs in these systems, which can significantly reduce the configurational entropy. We show that this cation order is not related to the difference in the oxidation state of the cations.

In the last part of this work, we show that the voltage of $(Mg_{0.2}Co_{0.2}Ni_{0.2}Cu_{0.2}Zn_{0.2})O$ can be tuned through a composition variation revealing the source of the Na inactivity with this material. We demonstrate that the origin of this inactivity is related to the voltage change when switching from a lithium-ion cell to a sodium-ion cell.

II. Methods

Synthesis of quenched samples. The precursors MgO (Sigma Aldrich, 99.9%), CoO (Alfa Aesar, 99.99%), NiO (Sigma Aldrich, 99.9%), CuO (Sigma Aldrich, 99.9%), and ZnO (Alfa Aesar, 99.9%) were massed and thoroughly mixed in an agate mortar. The mixed sample was separated into 1.00 g samples and pressed into 14.85 mm diameter pellets using a uniaxial hydraulic press (Carver) at 8 metric tons. The pellets were heated in air using a Lindberg Tube Furnace in a quartz glass boat for 20 h. The red-hot pellets were quenched in air by rapidly transferring them onto a copper plate.

Powder X-ray diffraction measurements. Powder X-ray diffraction (XRD) patterns were collected using a Bruker D8 Advanced diffractometer with a copper K_α radiation source and an LYNXEYE detector having a fixed divergence slit (0.3°). The counting time was set to 1 s per point at 0.02° 2θ increment.

In situ data were collected with Bruker D8 Advanced diffractometer with Bragg-Brentano optics. The counting time was set to 1s per point at 0.02° 2θ increment. The mixed sample was placed in an alumina sample holder with a diameter of 17 mm and resistively heated using an Anton Paar TCU-1000N hot stage in air. The sample was

ramped at a constant rate of 30 °C min^{-1} to a specified temperature and equilibrated for 3 h. XRD patterns were collected at the end of the 3 h equilibration time.

X-ray photoelectron spectroscopy (XPS) measurements. Samples were analyzed using X-ray photoelectron spectroscopy (XPS) to gain insight into the varying oxidation states of the metals in the materials. All samples were collected on the NEXSA G2 (Thermo Scientific) with an Al Kα source (1486.6 eV). Survey spectra were collected for all samples (Pass Energy 100, Step Size 1.0 eV, and dwell time 10 ms for 2 scans). High-resolution spectra for Mg 1s, Co 2p, Ni 2p, Cu 2p, Zn 2p, C 1s, and O 1s were also obtained (Pass Energy 50, Step Size 0.1, and dwell time 50 ms for 8 scans each). Due to the insulating nature of the samples, all spectra were collected with the charge compensation flood gun (200 μA). All spectra are calibrated to the aliphatic carbon feature (284.6 eV). Casa XPS software (Version 2.3.25) was used for the data analysis with either Shirley or Linear background subtraction.

X-ray absorption spectroscopy (XAS) measurements. X-ray absorption fine structure (XAFS) was measured at 8C nano-probe XAFS beamline (BL8C) of Pohang Light Source (PLS-II) in the 3.0 GeV storage ring, with a ring current of 250 mA. The X-ray beam was monochromated by a Si(111) double crystal, where the beam intensity was reduced by 30% to eliminate the higher-order harmonics. The X-ray beam was then delivered to a secondary source aperture where the beam size was adjusted to be 0.5 mm (v) × 1 mm (h). XAFS spectra were collected in transmission mode. The obtained spectra were processed using Athena software.

Electrode preparation. The synthesized single-phase materials were ground in an agate mortar and ball-milled for 3 h using a Deco-PBM-V-0.4L vertical lab planetary ball miller (Hanchen Instrument), with alumina as the milling media and a 3:1 ball (3 mm diameter) to powder ratio. Slurries composed of 65%, 25%, and 10% by weight of the ball-milled active material, carbon black (Carbon Vulcan Black XC-72R), and polyvinylidene fluoride (PVDF, MTI Corp.), respectively, were prepared using N-methyl-2-pyrrolidone (NMP, MTI Corp.) as a solvent. The slurry was cast onto a thin copper foil (9 μm, MTI Corp.) current collector using an adjustable doctor blade (MSK-AFA I, MTI CORP.). The coated foil was then dried at 65 °C in air for 4 h, followed by overnight drying at 100 °C under vacuum to completely remove any residual solvent. 12.7 mm diameter electrodes were cut out, each with a loading of about 1.5 mg cm^{-2}. A 1 M solution of sodium hexafluorophosphate ($NaPF_6$) in a 1:1 volume ratio of ethylene carbonate (EC) and dimethyl carbonate (DMC) was used as the electrolyte (MSE Supplies). Coin-type cells were assembled with 400 μm thick Na metal foil (Alfa Aesar, 99.9%) and glass microfiber separator (Sigma Aldrich, Whatman GF/A) inside an argon-filled glovebox (mBraun, [O_2] < 0.5 ppm, [H_2O] < 0.5 ppm).

The electrodes used for the XAS measurements were free-standing electrodes. The slurry comprised 75%, 15%, and 10% by weight of the ball-milled active material, carbon black, and PVDF, respectively. The slurry was cast onto a thin aluminum foil and dried at 65 °C in air for 8 h, followed by overnight drying at 100 °C under vacuum. The

aluminum foil was peeled off, and a free-standing electrode was obtained. 12.7 mm diameter electrodes were cut out, each with a loading of about 10.14 mg cm^{-2}. Coin-type cells were made. The cell was assembled as described above using a Celgard® 2400 separator, and the cycled electrodes were sandwiched between 2 Kapton tapes in an argon-filled glovebox for XAS measurements.

Electrochemical Characterization. Galvanostatic charge/discharge measurements were performed at room temperature using a battery testing system 8.0 (Neware). Cyclic voltammogram (CV) measurements were conducted at room temperature using a VMP3 multichannel potentiostat (BioLogic). All capacity measurements were normalized to the mass of the active material.

III. Results and Discussion

A. The role of configurational entropy in stabilizing the single-phase $(Mg_{0.2}Co_{0.2}Ni_{0.2}Cu_{0.2}Zn_{0.2})O$ compound

$(Mg_{0.2}Co_{0.2}Ni_{0.2}Cu_{0.2}Zn_{0.2})O$ composition variation and their transition temperatures. $(Mg_{0.2}Co_{0.2}Ni_{0.2}Cu_{0.2}Zn_{0.2})O$, $(Co_{0.25}Ni_{0.25}Cu_{0.25}Zn_{0.25})O$, $(Mg_{0.25}Ni_{0.25}Cu_{0.25}Zn_{0.25})O$, $(Mg_{0.25}Co_{0.25}Cu_{0.25}Zn_{0.25})O$, $(Mg_{0.25}Co_{0.25}Ni_{0.25}Zn_{0.25})O$, and $(Mg_{0.25}Co_{0.25}Ni_{0.25}Cu_{0.25})O$ were prepared in this work via a solid-state synthesis method, and is coded as TM-HEO, TM-MEO(-Mg), TM-MEO(-Co), TM-MEO(-Ni), TM-MEO(-Cu), and TM-MEO(-Zn) respectively henceforth. As noted, the compositions TM-MEO(-X), where "X" denotes the element removed, were prepared by omitting the binary oxide of that element from the composition used to prepare TM-HEO. The pellets of these materials were equilibrated for 20 hours at each temperature in an air tube furnace and quenched to room temperature. These materials were heated in 50 ^oC increments, and the temperature range is specific to each composition (Fig. 1). X-ray diffraction (XRD) measurements were used to monitor the phase evolution in these compounds and the results are depicted in Figure 1. Figure 1A shows the transition temperature of TM-HEO from a multiphase composition to a single-phase material (indexed to a rock salt phase) between 850 ^oC and 900 ^oC, corroborating Rost *et al.* [ref.[9]] findings. TM-MEO(-Mg) (Fig. 1B) transition from a multiphase mixture to a single-phase material at the same temperature interval as TM-HEO. TM-MEO(-Co) has a transition temperature between 1000 ^oC and 1050 ^oC (Fig. 1C), and the compositions TM-MEO(-Ni) (Fig. 1D and Fig. S2A), TM-MEO(-Cu) (Fig. 1E), and TM-MEO(-Zn) (Fig. 1F) all show the same transition temperature between 900 ^oC to 950 ^oC.

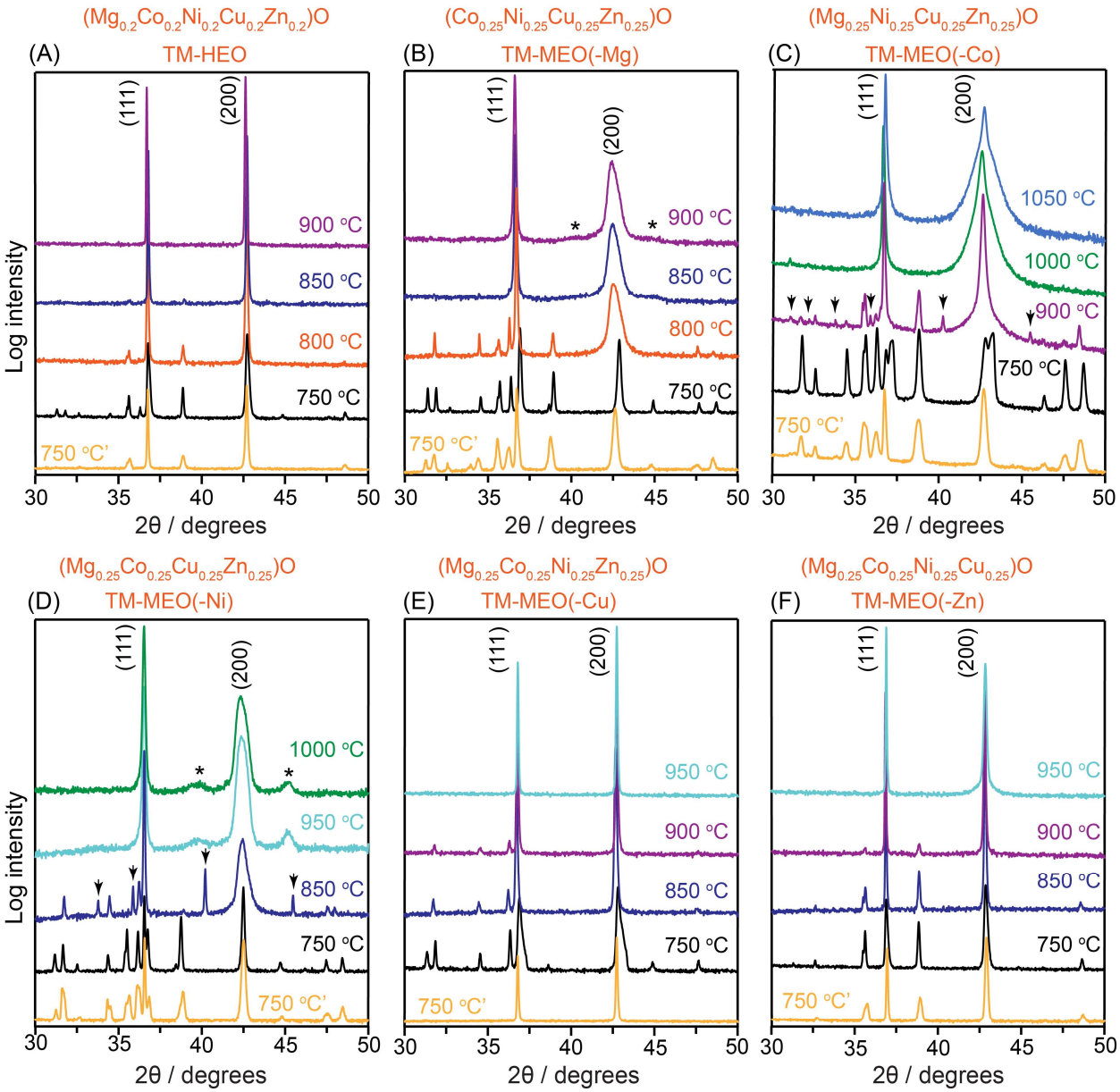

Figure 1. XRD patterns of the as-prepared materials at various temperatures for (A) $(Mg_{0.2}Co_{0.2}Ni_{0.2}Cu_{0.2}Zn_{0.2})O$ (TM-HEO), (B) $(Co_{0.25}Ni_{0.25}Cu_{0.25}Zn_{0.25})O$ (TM-MEO(-Mg)), (C) $(Mg_{0.25}Ni_{0.25}Cu_{0.25}Zn_{0.25})O$ (TM-MEO(-Co)), (D) $(Mg_{0.25}Co_{0.25}Cu_{0.25}Zn_{0.25})O$ (TM-MEO(-Ni)), (E) $(Mg_{0.25}Co_{0.25}Ni_{0.25}Zn_{0.25})O$ (TM-MEO(-Cu)), (F) $(Mg_{0.25}Co_{0.25}Ni_{0.25}Cu_{0.25})O$ (TM-MEO(-Zn)). The bottom XRD patterns labeled 750 °C' in all these figure panels were obtained by heating the single-phase materials at 750 °C. The arrows in this figure denote the ternary compound Cu_2MgO_3, and the asterisks (*) denote peaks from a superstructure. X-ray intensity is plotted on a logarithmic scale.

The chemical equation below depicts the reaction from the binary metal oxides to the single-phase TM-HEO. The characteristics of these binary metal oxides are shown in Table S1. The "RS," "T," and "W" indices in this chemical equation stand for rock salt, tenorite, and wurtzite, respectively. Rost *et al*. [ref.[9]] claimed that the transition of TM-HEO from a multiphase composition to a single-phase material was driven by configurational entropy. Their argument relied on equation 1 below.

$MgO_{(RS)} + CoO_{(RS)} + NiO_{(RS)} + CuO_{(T)} + ZnO_{(W)} = (Mg, Co, Ni, Cu, Zn)O_{(RS)}$

$$\Delta G = \Delta H - T\Delta S \dots\dots\dots\dots\dots\dots\dots\dots 1$$

Where ΔG is the reaction Gibbs free energy, ΔH is the heat of reaction (enthalpy), T is the temperature, and ΔS is the entropy change with respect to the individual binary oxides. Employing an ideal mixing assumption, they proposed that the change in entropy is dominated by the configurational entropy (that is, $\Delta S = \Delta S_{(conf.)}$). Using equation S1 (supplementary information), they calculated $\Delta S_{(conf.)}$ for TM-HEO to be 1.61R (R is the gas constant) and 1.39R for the rest of the quaternary metal oxides presented above. On the other hand, ΔH is referred to as the enthalpy of mixing, and it is generally expressed as shown in equation 2 [ref.[23]].

$$\Delta H_{(mixing)} = x\Delta H_{trans} + x(1-x)f(x) \dots\dots\dots\dots\dots\dots\dots\dots 2$$

Where $\Delta H_{(trans)}$ in this case, is the enthalpy of transformation of non-rock salt phases such as $CuO_{(T)}$ and $ZnO_{(W)}$ to their rock salt phases $CuO_{(RS)}$ and $ZnO_{(RS)}$ (that is $\Delta H_{trans} = \Delta H_{(W\ to\ RS)} + \Delta H_{(T\ to\ RS)}$). The second term is the generalized enthalpy of mixing, and x is the number of moles of the non-rock salt phase. In an ideal mixing assumption, the second term becomes zero, and equation 1 becomes:

$$\Delta G_{(mixing)} = x(\Delta H_{(W\ to\ RS)} + \Delta H_{(T\ to\ RS)}) - T\Delta S_{(config.)} \dots\dots\dots\dots\dots\dots\dots\dots\dots 3$$

McCormack and Navrotsky[24] have reported the ΔG_{trans} of ZnO and CuO to be about 24.26 kJ/mol and 22.20 kJ/mol, respectively. These are relatively large positive values, which is why Rost *et al*. [ref.[9]] claimed that the formation of TM-HEO is driven by entropy. They claimed that at the temperature where TM-HEO transforms into a single phase, none of the quaternary metal oxides could be prepared as a single phase due to their lower $\Delta S_{(conf.)}$. However, Fig. 1B shows that the quaternary metal oxide TM-MEO(-Mg) transitions at the same temperature as TM-HEO. The equilibration time they used in their work is 2 hours compared to the 40 hours (Fig. S1B) we used for TM-MEO(-Mg). We can thus conclude that the equilibration time was not long enough in their work to reach the thermodynamic equilibrium. Not only does the $\Delta S_{(conf.)}$ decrease from 1.61R in TM-HEO to 1.39R in TM-MEO(-Mg), but the "xΔH(trans)" term also increases due to a 25% increase in the number of moles of CuO and ZnO going from TM-HEO to TM-MEO(-Mg). This means that if the terms in equation 3 are all that is needed to describe the energetic landscape of these materials, TM-MEO(-Mg) composition should only be able to transition from a multiphase system to a single-phase material at a temperature higher than the transition temperature of TM-HEO. So, the simple fact that TM-HEO transitions to a

single-phase at the same temperature as TM-MEO(-Mg) indicates a much more complex energy landscape in these materials. In addition, TM-MEO(-Mg), TM-MEO(-Co), and TM-MEO(-Ni) all transition to single-phase materials at different temperatures, which hints at an energy landscape that is dependent on the nature of the individual binary oxide component rather than the number of components. What is even more telling is that TM-MEO(-Cu) and TM-MEO(-Zn) transition to single-phase materials at a higher temperature than TM-MEO(-Mg) and at the same temperature as TM-MEO(-Ni). This is surprising because about a 50% decrease in "$x\Delta H_{(trans)}$" is expected as one removes either CuO or ZnO, which should lead to a lower transition temperature for TM-MEO(-Cu) and TM-MEO(-Zn) relative to the remaining quaternary oxides.

A clear sign of non-ideal mixing contributions in these materials is the formation of the Guggenite phase ($MgCu_2O_3$) [ref.[25,26]], indicated in Figure 1 by the arrows. This phase is stabilized at 850 ºC for TM-MEO(-Ni) (Fig. 1D and Fig. S2A) and at 900 ºC for TM-MEO(-Co) (Fig. 1C and Fig. S2B). A CALPHAD assessment, which takes into account non-ideal mixing interactions, has predicted the formation of this ternary metal oxide phase at a copper mole fraction of about 0.22 and at a temperature of about 877 ºC in the system MgO-CuO [ref.[26-28]]. This CALPHAD assessment in the MgO-CuO system matches well with our experiments, suggesting complex non-ideal mixing interactions in these compounds. In addition, the lack of formation of this Guggenite phase in the TM-MEO(-Zn) system further suggests a complex interaction of cations in these compounds.

Annealing the single-phase materials at 750 ºC (XRD patterns labeled 750 ºC' in Fig. 1) for 20 hours led to the transition from single-phase to multiphase compositions. There is no doubt that reheating each of the multiphase compositions back to their transition temperature would have led to them transitioning again to single-phase materials since the XRDs of the 750 ºC' look very similar to that of 750 ºC. This phase reversibility, linked to the temperature cycle, was used by Rost *et al*. [ref.[9]] to justify that TM-HEO is entropy stabilized (see equation 3). However, Figure 1 shows that all quaternary metal oxides also demonstrate the same behavior except TM-MEO(-Cu) (Fig. 1E). TM-MEO(-Cu) remains a single-phase material after annealing at 750 ºC for 20 hours. We thus hypothesize that the transformation from single phase to multiphase in these systems is due to the strain introduced in these materials by the presence of copper in the octahedral environment. If we presuppose that copper in these materials is in a +2-oxidation state (d^9) and in an octahedral environment, then to lift its large electronic degeneracy, a distortion of its local coordination environment is necessary (Jahn-Teller effect)[29]. This will lead to an axial elongation or compression of the oxygen octahedron around the copper cation, causing this octahedron to become distorted. This distortion may introduce high strain in these materials to cause the observed phase transition below the consolute temperature. This is also likely why XRD patterns of all quaternary metal oxides single-phase materials with a high mole fraction of copper (0.25) show significant deviation from an ideal rock salt structure except TM-MEO(-Cu). This deviation from the ideal rock salt structure reveals itself in the XRD patterns of the copper-containing quaternary metal oxides through the significant broadening and lower intensity of the

(200) lattice plane relative to the (111) lattice plane. This selective peak broadening in the XRD pattern has also been observed in the TM-HEO system by gradually increasing the copper content[30].

Origin of peak broadening in the XRD patterns. Figure 2 shows the powder XRD patterns of all the materials. The 2θ range is expanded to 82° to include more peaks from these rack salt materials. To be clear, the "intensity" of a diffraction peak in this whole study refers for simplicity to its maximum value after background subtraction rather than the more accurate integrated intensity. Although the ratios $I_{(111)}/I_{(200)}$ are slightly different with the second definition, the conclusions that can be obtained from the diffraction patterns are exactly the same. With this definition, the ideal ratio should be 0.67. In the current study, this ratio changes depending on the composition of the material, as depicted in Figure 2. All quaternary metal oxides show significant deviation from the ideal ratio except TM-MEO(-Cu) ($I_{(111)}/I_{(200)}$ = 0.57). TH-HEO has a ratio of 0.84, which is close to the ideal ratio. However, after ball-milling (bottom panel of Fig. S3), a significant increase in this ratio is observed (1.19). This behavior has also been observed by slowly cooling this material from above its consolute temperature[30]. This indicates that the quenched TM-HEO is kinetically trapped at room temperature, giving the illusion of a thermodynamically stable material. The quenched form of TM-MEO(-Cu)

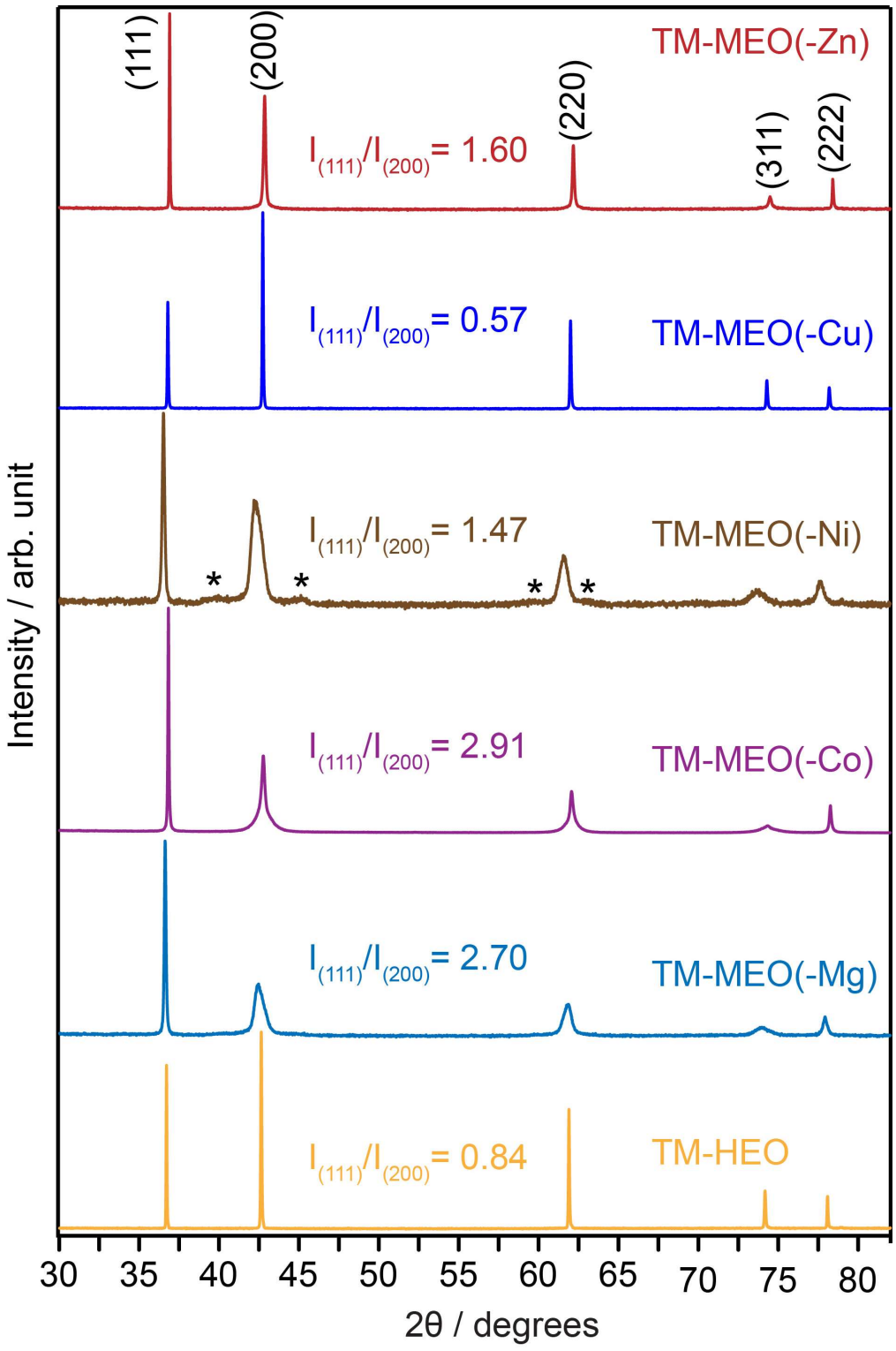

Figure 2. Powder XRD patterns of all the materials quenched in air above their consolute temperature. The 2θ range is expanded to 82° to include more lattice planes. The $I_{(111)}/I_{(200)}$ are the intensity ratios of the (111) and (200) lattice planes. The lattice parameter of all the samples is shown in Table S3.

is thus truly thermodynamically stable at room temperature since its XRD pattern does not change even after annealing at 750 °C for 20 hours (Fig. 1E). There is a clear (hkl)-dependent peak broadening on the XRD pattern of all materials except for TM-MEO(-Cu). While the <111> family of planes remains sharp, the (200), (220), and (311) planes are significantly broad. This has been attributed to a tetragonal distortion of the rock salt phase[23,30]. Bularzik *et al*. [ref.[23]] also observed this (hkl)-dependent peak broadening in the system NiO-CuO at a 0.35-mole fraction of copper and suggested that this tetragonal distortion was due to cation order. However, Berardan *et al*. [ref.[30]] claimed that this tetragonal distortion could not be attributed to cation ordering in TM-HEO since secondary peaks indicating the presence of a superstructure were not observed on the XRD pattern. The peaks labeled with black asterisks (*) in Figure 1B, 1D, and Figure S2 represent broad secondary peaks that first appear for TM-MEO(-Mg) at about 850 °C (Fig. 1B) and for TM-MEO-(Ni) at about 900 °C (Fig. S2A). The peaks become significantly intense for TM-MEO(-Ni) at about 950 °C and decrease with increased annealing temperature (Fig. S2A). We believe these diffuse peaks are part of a superstructure formed due to cation order[31,32]. This would explain why Berardan *et al*. [ref.[30]] were not able to simulate the powder XRD pattern of the slowly cooled TM-HEO with broad (200), (220), and (311) peaks by simply assuming a tetragonal or rhombohedral distortion. TM-MEO(-Co) and TM-MEO(-Zn) also show significant deviation from the ideal rock salt structure, but no diffuse secondary peaks were observed on their XRD patterns (Fig. 2). However, because they all show similar (hkl)-dependent broadening pattern, cation order must also be at the origin of this effect. This broadening effect due to cation ordering should disappear at high temperatures where cation disorder dominates.

Figure 3A, B, C, and D show the in situ XRD measurements of TM-HEO, TM-MEO(-Mg), TM-MEO(-Co), and TM-MEO(-Ni), respectively. The red asterisks (*) denote instrument artifacts and do not belong to any of the starting materials. The arrows are peaks from the Guggenite phase ($MgCu_2O_3$), already discussed earlier. Each spectrum was collected after a three hours rest at the specified temperature. TM-HEO and TM-MEO(-Mg) transition to a single phase at the same temperature, which matches the earlier experiments. This observation indicates that the twenty hours anneal time used for the quenched experiments is long enough to reach thermodynamic equilibrium. TM-MEO(-Ni) transitions to a single phase at 1000 °C, which is 50 °C higher than in the earlier experiment. This likely indicates slower kinetics in this system. TM-MEO(-Co) also shows slow kinetics and does not transition to a single phase at 1050 °C. The peak intensity patterns in these in situ measurements significantly change from what was observed with the quenched samples. The peak intensity ratios ($I_{(111)}/I_{(200)}$) in these in situ measurements approach that of the ideal rock salt. For example, $I_{(111)}/I_{(200)}$ changes from 1.47 in Fig. 2 to 0.61 for TM-MEO(-Ni). TM-MEO(-Mg) also changes from 2.70 to 0.69, and TM-HEO goes from 0.84 to 0.71. Although TM-MEO(-Co) does not transition to a single phase (Fig. 3C), it is evident that the (200) peak is not as broad as it is in Fig. 1C. It is important to note that the broad secondary peaks earlier identified as part of a superlattice for TM-MEO(-Mg) (Fig. 1B) and TM-MEO(-Ni) (Fig. 1D) are entirely absent from these in situ data. These results indicate that cations become highly disordered at high temperatures in

these systems as expected and highly ordered at room temperature to minimize the energy of these systems.

Figure 3E shows a series of samples prepared by substituting Mg in TM-HEO with Ca. The samples were heated at 1000 ^{o}C for twenty hours in air. The XRD patterns are for the quenched room-temperature samples. Ca residues are observed for samples with a Ca content of 0.2 and 0.16. At the same time, a single-phase material is obtained for the sample with a Ca content of 0.1 (Fig. 3E). The intensity ratio ($I_{(111)}/I_{(200)}$) = 0.67, which is precisely the ratio for an ideal rock salt structure. Ball milling the sample yields the XRD pattern in Figure S3 (top panel) with the $I_{(111)}/I_{(200)}$ = 0.91. This ratio is still close to the ideal rock salt ratio, unlike the case with TM-HEO. This result is quite surprising because Berardan *et al*. [ref.[29]] showed that significant peak broadening is observed on the XRD pattern of TM-HEO with similar copper content (0.22). Ca, with its large crystal radius (Table S1), seems to mitigate cation ordering in the $(Ca_{0.1}Co_{0.225}Ni_{0.225}Cu_{0.225}Zn_{0.225})O$ system similar to TM-MEO(-Cu). However, annealing at 750 ^{o}C for twenty hours leads to the transition from a single-phase material to a multiphase composition (Fig. 3E), unlike the TM-MEO(-Cu) material. All materials presented so far appear to show this phase transition from single-phase material to multiphase composition except the sample without copper (TM-MEO(-Cu)). This is further evidence that copper, via the Jahn-Teller effect, is mainly responsible for this phase transition rather than entropy.

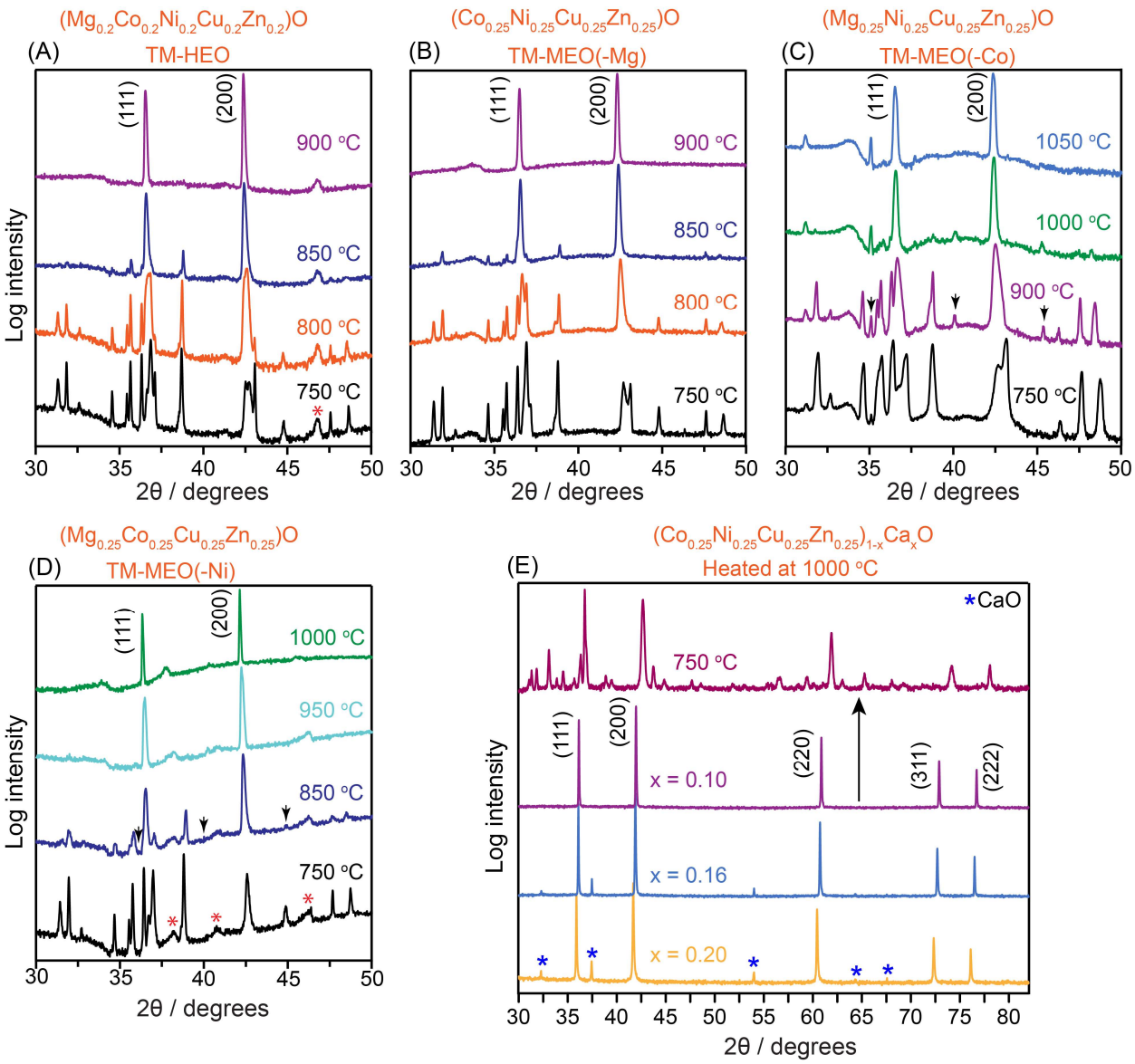

Figure 3. In situ powder XRD pattern of (A) TM-HEO, (B) TM-MEO(-Mg), (C) TM-MEO(-Co), and (D) TM-MEO(-Ni). These XRD patterns were measured at the specified temperatures. The arrows in these figures indicate the $MgCu_2O_3$ phase, and the asterisks (*) represent peaks that do not belong to any starting materials. (E) $(Co_{0.25}Ni_{0.25}Cu_{0.25}Zn_{0.25})_{1-x}Ca_xO$ samples heated at 1000 °C for 20 hours and quenched in air. The arrow shows the transition of the composition with x = 0.1 from the single phase to the multiphase after annealing at 750 °C for 20 hours. The asterisks (*) denote the residual peaks of CaO.

The difference in cation oxidation states is not responsible for cation order in these systems. It is well known that the difference in cation oxidation states can lead to cation

ordering in oxide compounds[24,33]. The compound, CoO, containing the redox-sensitive Co^{2+} species, can easily be oxidized to the more stable spinel Co_3O_4, generating the Co^{3+} cation in the process. On the other hand, the Cu^{2+} center in CuO can also be reduced to Cu^{1+} at elevated temperatures. For these reasons, X-ray photoelectron spectroscopy (XPS) measurements were performed on TM-HEO (Fig. 4A), TM-MEO(-Co) (Fig. 4B), and TM-MEO(-Mg) (Fig. 4C) to investigate the oxidation states of cations in these compounds. The O 1s spectra (Fig. S4 and Table S4,5 and 6) were deconvoluted into a metal-oxygen peak at 529.4 eV, 529.1 eV, 529.4 eV, a metal-hydroxide peak at 531.4 eV, 531.2 eV, 531.3 eV, and an adsorbed water peak at 533.0 eV, 533.6 eV, none for TM-HEO, TM-MEO(-Co), and TM-MEO(-Mg) respectively. The Mg 1s peak at about 1303.6 eV and 1303.4 eV for TM-HOE (Fig. 4A) and TM-MEO(-Co) (Fig. 4C), respectively, fit a single peak corresponding to Mg^{2+}. The Co $2p_{1/2}$ and $2p_{3/2}$ at 796.1 and 780.3 eV, 796.0 and 780.1 eV for TM-HEO (Fig. 4A) and TM-MEO(-Mg) (Fig. 4A), respectively, and their corresponding satellite peaks are fit to a single Co^{2+} oxidation state. The Ni $2p_{3/2}$ and $2p_{1/2}$ peaks at 855.2 and 872.8 eV for TM-HEO, 855.1 and 872.8 eV for TM-MEO(-Co), and 855.1 and 872.7 eV for TM-MEO(-Mg), with their corresponding satellite peaks fit to a single peak corresponding to the Ni^{2+} oxidation state (Fig. 4). The Cu $2p_{3/2}$ and $2p_{1/2}$ peaks at 933.7 and 953.3 eV for TM-HEO, 933.2 and 953.0 eV for TM-MEO(-Co), and 933.5 and 953.2 eV for TM-MEO(-Mg), with their corresponding satellite peaks fit to a single peak corresponding to the Cu^{2+} oxidation state (Fig. 4). Finally, the peak fit for the Zn $2p_{3/2}$ and $2p_{1/2}$ peaks at 1021.3 and 1044.4 eV for TM-HEO, 1021.2 and 1044.3 eV for TM-MEO(-Co), and 1021.2 and 1044.3 eV for TM-MEO(-Mg), with their satellite peaks indicate that Zn is in a +2 oxidation state (Fig. 4). The fitting parameters for these XPS data can be found in Table S4, 5, and 6 of the supplementary information. This surface analysis indicates that all metal cations are in their +2 oxidate state. X-ray absorption near edge structure (XANES) and extended X-ray absorption fine structure (EXAFS) data were collected to gain more insight into the cation oxidation states in the bulk and their local coordination environment.

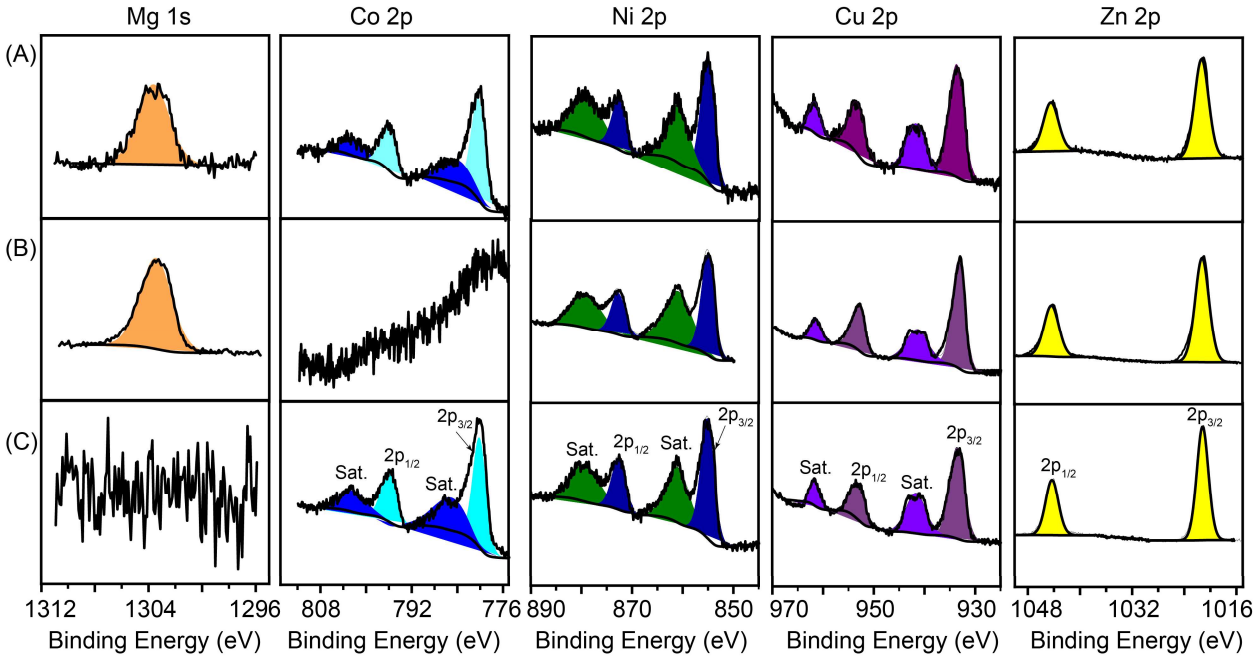

Figure 4. X-ray photoelectron spectroscopy (XPS) of (A) TM-HEO, (B) TM-MEO(-Co), and (C) TM-MEO(-Mg).

X-ray absorption spectroscopy (XAS) results, including XANES and extended X-ray absorption fine structure Fourier transforms (EXAFS-FT) of the K-edge of Co, Ni, Cu, and Zn, are shown in Figure 5 (also see the XANES derivative plots in Fig. S5). The K-edges of Co, Ni, and Cu in these prepared materials look very similar to their reference compounds, indicating that their oxidation states remain +2, corroborating the XPS results. On the other hand, the K-edge of Zn appears shifted to higher energies in these materials relative to its reference compound. This shift might indicate an increase in the oxidation state of Zn cation in these prepared samples. However, one must consider that Zn in ZnO is in a tetragonal environment compared to the octahedral environment it occupies in these multimetal oxides. This change in the coordination environment is more likely responsible for the observed energy shift rather than an increase in oxidation number. The Zn 2p XPS date corroborates this hypothesis. Both surface analysis (XPS) and bulk material analysis (XANES) techniques provide clear evidence that all cations in TM-HEO, TM-MEO(-Co), and TM-MEO(-Mg) are in the same oxidation station. We can thus conclude that a difference in the oxidation state of cations is not responsible for the ordering of cations in these materials.

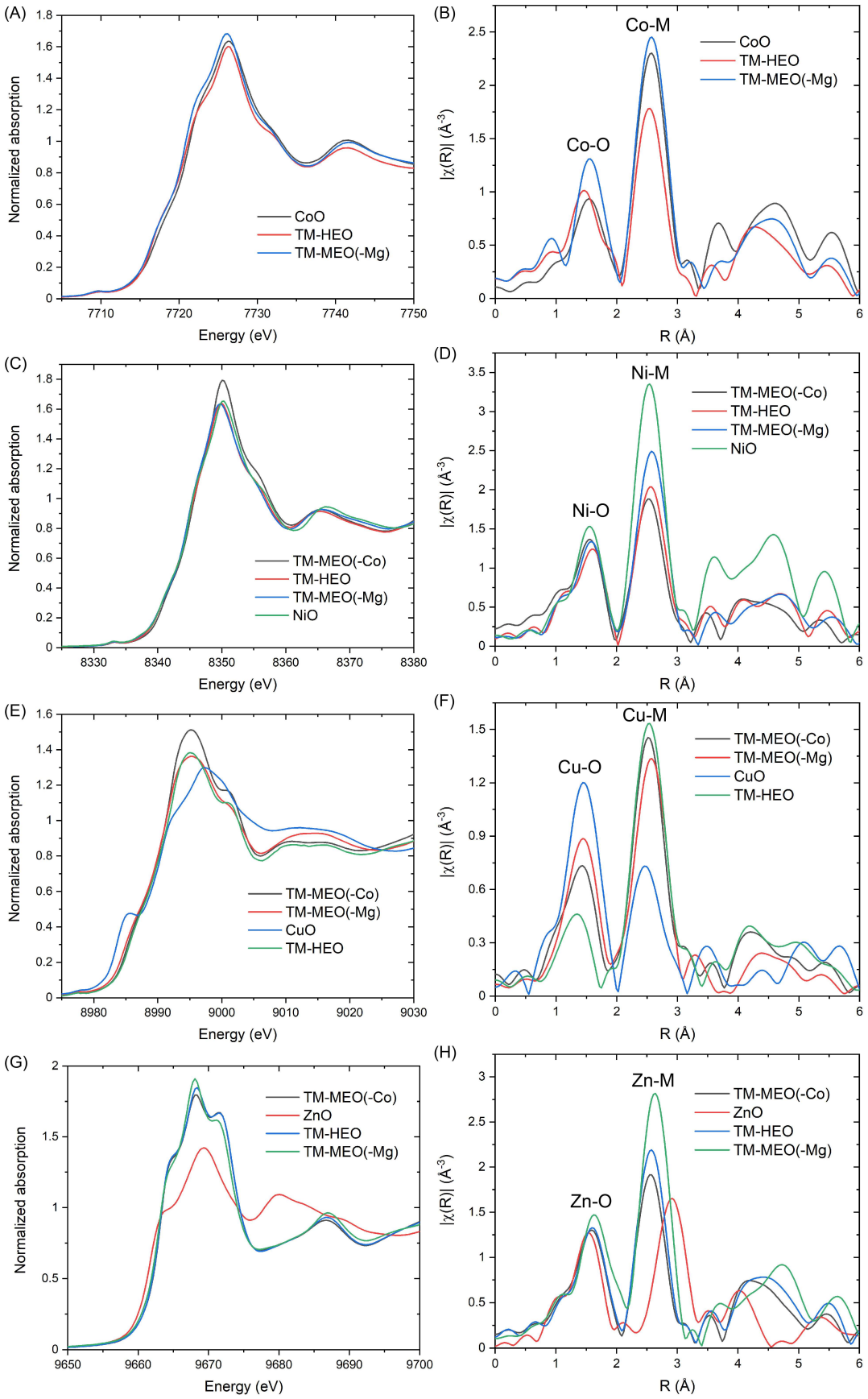

Figure 5. Valence state and atomic coordination analysis. (A), (C), (E), (G) XANES K-edge data for Co, Ni, Cu, and Zn. (B), (D), (F), (H) corresponding EXAFS-FT. The binary oxides data in these figures are for reference samples provided by the beamline.

Local coordination analysis reveals cation order. EXAFS-FT data were collected for Co, Ni, Cu, and Zn; the results are shown in Figure 5B, D, F, and H, respectively. Tables S7 and 8 present a global summary of these EXAFS-FT results. The Cu pre-edge peak observed for CuO completely disappears in the K-edge spectra of TM-HEO, TM-MEO(-Co), and TM-MEO(-Mg). This disappearance clearly indicates a switch in Cu's coordination environment. Similarly, the average bond distance for the Zn-to-metal second-near-neighbor in ZnO changes from 3.072 Å in ZnO to 2.571 Å in TM-HEO, 2.624 Å in TM-MEO(-Mg), and 2.571 Å in TM-MEO(-Co). This significant bond distance change and the Zn K-edge shift discussed earlier indicate a change in Zn's coordination environment. The signal pattern between 3 to 6 Å for the NiO and CoO reference can indicate the octahedral environment of these cations in a rock salt structure. Since these same features are observed for the EXAFS-FT data of Zn and Cu (Fig. 5F and H, respectively) in TM-HEO, TM-MEO(-Co), and TM-MEO(-Mg), we conclude that Cu and Zn are in an octahedral environment in these materials. The cation-to-anion (M-O) first-near-neighbor average distances in TM-HEO are 1.456, 1.611, 1.356, and 1.611 Å for Co-O, Ni-O, Cu-O, and Zn-O, respectively. Similarly, the average distances for the cation-to-cation (M-M) second-near-neighbor are 2.571, 2.545, 2.571, and 2.545 Å for Zn-M, Cu-M, Ni-M, and Co-M, respectively. Clearly, these average bond distances for the first and second-near-neighbors are not identical. Similar results are obtained with TM-MEO(-Co) and TM-MEO(-Mg), which unambiguously indicates that cations are not randomly distributed in these materials as opposed to the conclusion by Rost et al. [ref.[9]]. This observed cation order effectively decreases the configurational entropy contribution compared to ideal mixing. These conclusions stress the need to include non-ideal mixing terms in equation 3 to describe the energy landscape in these complex materials fully.

B. Voltage tuning via compositional variation of the $(Mg_{0.2}Co_{0.2}Ni_{0.2}Cu_{0.2}Zn_{0.2})O$ material and the benefits in sodium ion battery

Thermodynamics explains the Na inactivity with $(Mg_{0.2}Co_{0.2}Ni_{0.2}Cu_{0.2}Zn_{0.2})O$. The electrochemical performance of TM-HEO, TM-MEO(-Mg), and $(Ca_{0.1}Co_{0.225}Ni_{0.225}Cu_{0.225}Zn_{0.225})O$ in sodium ion battery was evaluated in a CR2032 coin-type battery geometry with Na-metal as the counter electrode using galvanostatic cycling. A typical loading in this work was about 1.5 mg of active material per cm^2 except otherwise specified. The specific capacity versus cycle number at various current densities are shown in Figure 6A, B, and C for TM-HEO, TM-MEO(-Mg), and $(Ca_{0.1}Co_{0.225}Ni_{0.225}Cu_{0.225}Zn_{0.225})O$, respectively. TM-HEO demonstrates poor electrochemical performance relative to TM-MEO(-Mg) and

($Ca_{0.1}Co_{0.225}Ni_{0.225}Cu_{0.225}Zn_{0.225}$)O. TM-MEO(-Mg) and ($Ca_{0.1}Co_{0.225}Ni_{0.225}Cu_{0.225}Zn_{0.225}$)O show similar electrochemical performance data. TM-HEO has previously demonstrated outstanding electrochemical performance in lithium-ion battery application[7,22,34]. Ghigna *et al*. [ref.[22]] attempted to provide a plausible explanation for this outstanding electrochemical performance by investigating the lithium storage mechanism in this material. They concluded that TM-HEO stores lithium via the reversible formation and removal of the Li_xZn and Li_xMg intermetallic phases after the first discharge cycle. In addition, they also suggested that the failure of TM-HEO material to store Na ions originates from the fact that Na does not form any intermetallic phases with Zn and Mg. This argument cannot be valid as TM-MEO(-Mg) shows some electrochemical activity with Na, albeit with poor long-term electrochemical performance. A likely explanation was proposed by Klein *et al*. [ref.[35]] using first principle thermodynamic calculations in the binary metal chalcogenide and halide systems. They concluded that replacing Li with Na leads to a constant shift in cell potential $\Delta E^o_{(Li\text{-}Na)}$, depending on the material class for a given conversion electrode material. This shift in cell potential was evaluated to be about 0.96 V for the metal oxides class. Figure 6G shows the voltage profiles versus Li/Li^+ of TM-HEO, TM-MEO(-Mg), TM-MEO(-Co), and ($Ca_{0.1}Co_{0.225}Ni_{0.225}Cu_{0.225}Zn_{0.225}$)O. This voltage profile shows two plateau series at about 0.70 V for TM-HEO and TM-MEO(-Co) and another at about 1.00 V for TM-MEO(-Mg) and ($Ca_{0.1}Co_{0.225}Ni_{0.225}Cu_{0.225}Zn_{0.225}$)O. TM-HEO and TM-MEO (-Co) (Fig. S6) show no activity with Na, while TM-MEO(-Mg) and ($Ca_{0.1}Co_{0.225}Ni_{0.225}Cu_{0.225}Zn_{0.225}$)O show some electrochemical activity. Figure 6H shows the voltage profile of TM-MEO(-Mg) and ($Ca_{0.1}Co_{0.225}Ni_{0.225}Cu_{0.225}Zn_{0.225}$)O versus Na/Na^+. This voltage profile shows a sloping voltage region from about 0-200 mAh g^{-1} and a plateau at about 0.04 V. We assign this sloping region to the conductive carbon black (Fig. S6) and the plateau to the electrochemical activity of TM-MEO(-Mg) and ($Ca_{0.1}Co_{0.225}Ni_{0.225}Cu_{0.225}Zn_{0.225}$)O with Na. These results provide a $\Delta E^o_{(Li\text{-}Na)}$ value of exactly 0.96 V, as calculated by Klein *et al*. [ref.[35]]. So, from these results, TM-HEO and TM-MEO(-Co) should show some activity in a Na-ion cell at about -0.26 V versus Na/Na^+. However, even if one were to shift the lower voltage limit to below -0.26 V versus Na/Na^+, Na plating, which is kinetically favorable, would occur. This is why TM-HEO and TM-MEO(-Co) remain electrochemically inactive in a sodium-ion cell while TM-MEO(-Mg) and ($Ca_{0.1}Co_{0.225}Ni_{0.225}Cu_{0.225}Zn_{0.225}$)O show some activity. As presented above, this ability to tune the voltage profile is a significant advantage of these complex multimetal compounds.

Figure 6D, E, and F show the differential capacity plots for TM-HEO, TM-MEO(-Mg), and ($Ca_{0.1}Co_{0.225}Ni_{0.225}Cu_{0.225}Zn_{0.225}$)O, respectively. As expected, TM-HEO shows no electrochemical activity, while TM-MEO(-Mg) and ($Ca_{0.1}Co_{0.225}Ni_{0.225}Cu_{0.225}Zn_{0.225}$)O show similar electrochemical profiles. This implies that the (de)sodiation mechanism in TM-MEO(-Mg) is the same as in ($Ca_{0.1}Co_{0.225}Ni_{0.225}Cu_{0.225}Zn_{0.225}$)O.

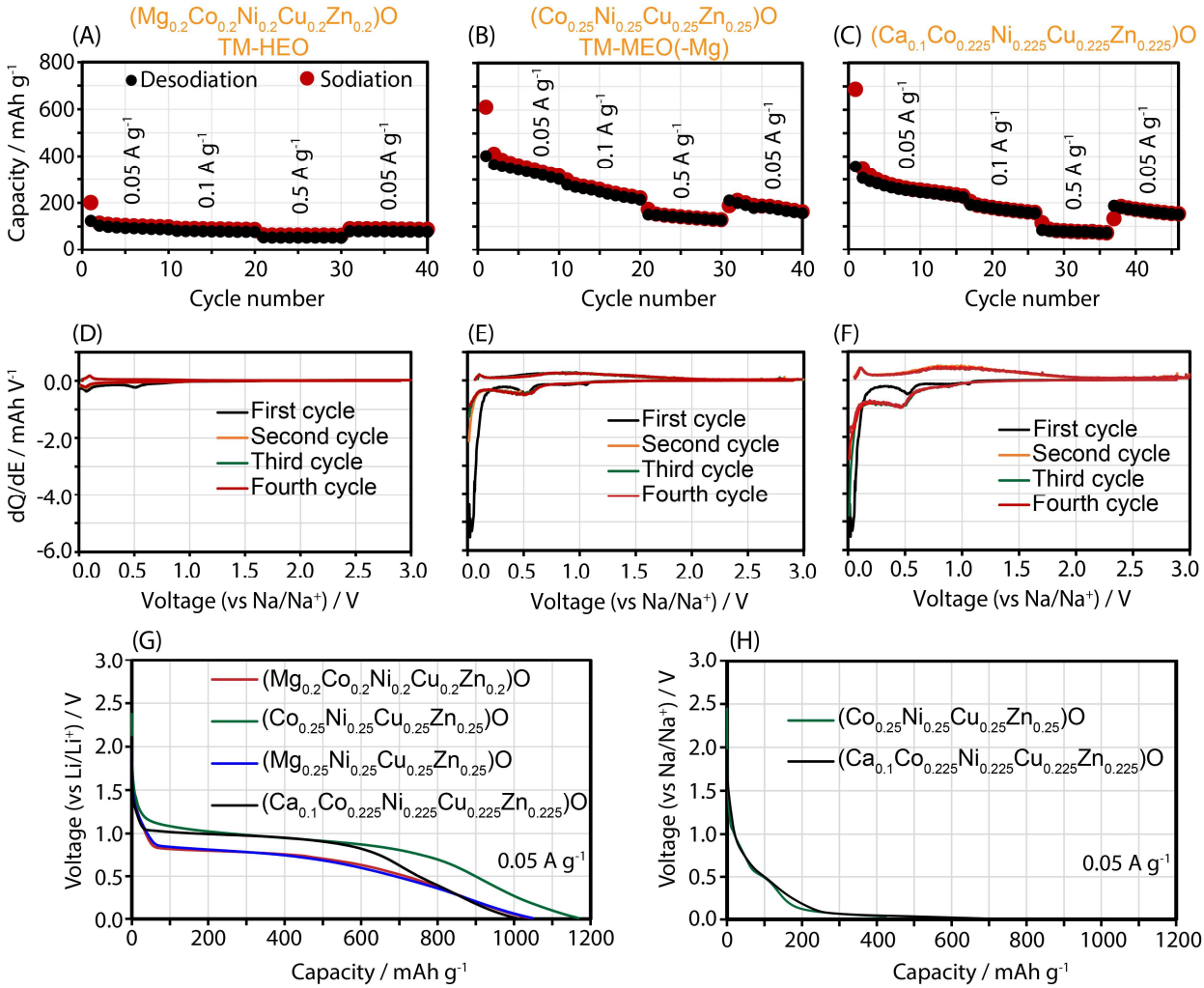

Figure 6. **Electrochemical characterization of TM-HEO, TM-MEO(-Mg), and $(Ca_{0.1}Co_{0.225}Ni_{0.225}Cu_{0.225}Zn_{0.225})O$.** (A-C) Specific capacity plots at various current densities for TM-HEO (A), TM-MEO(-Mg) (B), and $(Ca_{0.1}Co_{0.225}Ni_{0.225}Cu_{0.225}Zn_{0.225})O$ (C). (D-F) Differential capacity plots for TM-HEO (D), TM-MEO(-Mg) (E), and $(Ca_{0.1}Co_{0.225}Ni_{0.225}Cu_{0.225}Zn_{0.225})O$ (F). These dQ/dE plots were obtained at a current density of 0.05 A g^{-1}. (G, H) Voltage profiles of specified materials versus Li/Li^+ half cell (G) and Na/Na^+ half cell (H). All the data collected here were within a 0.01-3.00 V voltage window. Typical loading was 1.5 mg cm^{-2} except otherwise specified.

The partial sodiation of TM-MEO(-Mg). A free-standing (no current collector) electrode of TM-MEO(-Mg) with a thickness of 68.40 µm and a loading of 10.14 mg cm^{-2} was cycled from 3.00 V to 0.01 V at a 0.1 mV s^{-1} scan rate. The electrode was then held at 0.01 V for 148 hours to allow the reaction to reach a thermodynamic equilibrium (Fig. S7). Figure 7 shows the XANES and EXAFS-FT of the K-edge of Co, Ni, Cu, and Zn. All cations in a fresh (non-cycled) electrode (denoted TM-MEO(-Mg)_NS in the figure) are in a +2 oxidation state as previously determined. After the discharge of the electrode to 0.01 V

(denoted TM-MEO(-Mg)_S in Fig. 7), the XANES K-edge of Co, Ni, and Zn (Fig. 7A, C, and G) does not differ from the non-cycled electrode. The XANES derivative plots (Fig. S8) for these elements also do not show any shift in the K-edge. The EXAFS-FT of the K-edge of Co, Ni, and Zn (Fig. 7B, D, and H) also shows no change in the valence state and coordination environment relative to the non-cycled electrode. These are indications that Co, Ni, and Zn do not participate in the electrochemical reaction of TM-MEO(-Mg) with Na. On the other hand, the XANES K-edge of Cu (Fig. 7E) for the discharged cell shows a pre-edge peak that matches well with the pre-edge of the Cu foil reference. This is more prominent on the XANES K-edge derivative plot (Fig. S8C). The EXAFS of the Cu K-edge for the cycled electrode (Fig. 7F) shows a shift of the average bond distance of Cu-M toward a lower value closer to the Cu-Cu bond distance of the Cu foil reference. A slight decrease in the intensity of the Cu-O first coordination shell peak is also observed for this cycled electrode, which indicates that oxygen was removed from the coordination shell of Cu. These observations imply that the reaction of TM-MEO(-Mg) with Na involves the reduction of Cu^{2+} to Cu^{o}. However, since the Cu-M peak in the EXAFS K-edge of the cycled electrode does not match that of the Cu-Cu peak for the Cu foil reference and a complete removal of oxygen from the coordination shell of Cu is not observed, we conclude that not all the Cu^{2+} in TM-MEO(-Mg) gets reduced to Cu^{o}. A similar cycled electrode was analyzed using XRD to further show the extent of this partial reaction of TM-MEO(-Mg) with Na (Fig. S9). One can clearly see that a significant fraction of TM-MEO(-Mg) is left unreacted after holding the electrode at 0.01 V for 148 hours. This partial reaction of Na with metal oxides has been well studied in the NiO system[36]. It was suggested that the thicker Na_2O layer formed at the surface of metal oxide particles during sodiation compared to lithiation impedes the transport of Na^{+}, thus preventing the full sodiation of the oxide particle.

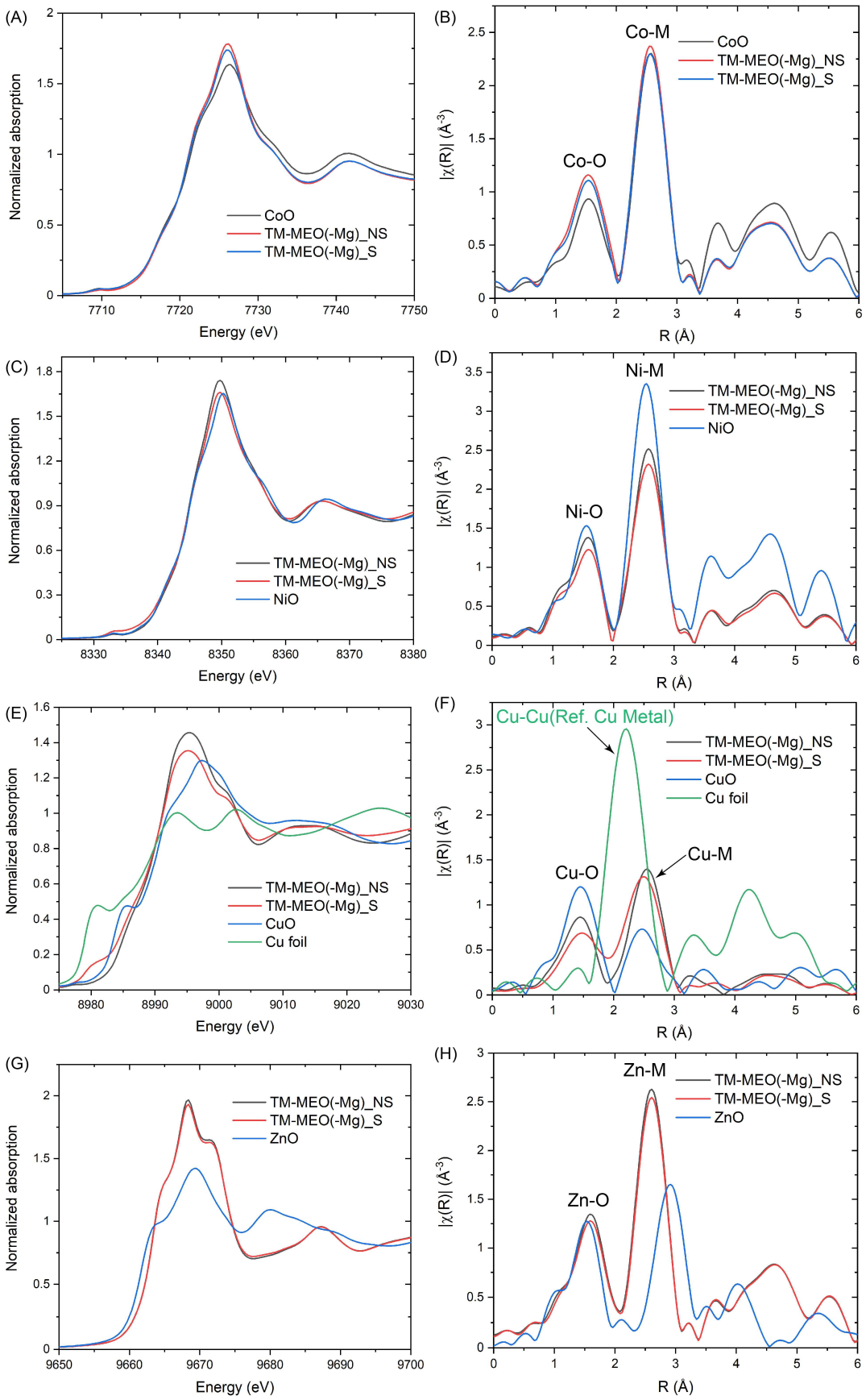

Figure 7. **Valence state and atomic coordination analysis of sodiated and non-sodiated TM-MEO(-Mg) electrode**. (A), (C), (E), (G) XANES K-edge data for Co, Ni, Cu, and Zn. (B), (D), (F), (H) corresponding EXAFS-FT. The binary oxides and copper foil data in these figures are for reference samples provided by the beamline. TM-MEO(-Mg)_NS is the fresh (non-cycled) electrode of TM-MEO(-Mg), while TM-MEO(-Mg)_S is the sodiated electrode.

IV. Summary

TM-MEO(-Mg), TM-MEO(-Co), TM-MEO(-Ni), TM-MEO(-Cu), and TM-MEO(-Zn) were prepared by omitting the binary oxide of the element in the bracket from the composition of TM-HEO. Their consolute temperature was determined to evaluate the role of configurational entropy in stabilizing the single-phase TM-HEO. It was demonstrated that the consolute temperature of these materials does not depend on the number of components but rather on the nature of the components. This highly contradicts the ideal mixing of cations assumption proposed in previous research. The transition temperature of TM-HEO and TM-MEO(-Mg) was observed to be the same despite the 25% increase in the mole fraction of the non-isostructural components, CuO and ZnO. This implies that the thermodynamic energy landscape cannot simply be described by assuming an ideal mixing of cations. Similar observations were made for TM-MEO(-Ni), TM-MEO(-Cu), and TM-MEO(-Zn) since these three materials showed the same transition temperature despite the decrease in the mole fraction of the non-isostructural components Zn or Cu. The fact that TM-MEO(-Mg) transitions to a single phase at a lower temperature than TM-MEO(-Cu) and TM-MEO(-Zn) further justified that the mixing of cations in these compounds is non-ideal. These non-ideal interactions reveal themselves via the (hkl)-dependent peak broadening and the formation of a superstructure, which are telltale signs of cation order in a crystalline material. This cation order was shown to disappear at high temperatures, as expected, where cation disorder dominates. Using XPS and XAS, we showed that this cation order is not caused by the difference in the oxidation state of cations but rather by the complex interaction between components to minimize the system's overall energy. The detection of cation order in these systems highly weakens the conclusion that configurational entropy is the main driving force in stabilizing these materials to a single phase at room temperature. The transition from a single-phase material to a multi-component mixture below the consolute temperature has been used as solid evidence of entropy stabilization in these systems. However, we have demonstrated that this transition may be caused by the strain introduced in the material by the distorted octahedron around the copper center due to the Jahn-Teller effect. These observations stress that only with sufficient thermodynamic characterization to show that the entropy of formation dominates over the enthalpy of formation can an oxide be rigorously classified as a high entropy oxide.

Through thermodynamic calculations, it has been demonstrated that replacing Li with Na leads to a constant shift in cell potential $\Delta E^{o}_{(Li\text{-}Na)}$, depending on the

material class for a given conversion electrode material. This shift in cell potential was evaluated to be about 0.96 V for the metal oxides class. The voltage profile for the first discharge cycle of TM-HEO and TM-MEO(-Co) shows a plateau at about 0.70 V versus Li/Li^+ and 1.00 V for TM-MEO(-Mg) and $(Ca_{0.1}Co_{0.225}Ni_{0.225}Cu_{0.225}Zn_{0.225})O$. This means that the shift in cell potential $\Delta E^o_{(Li-Na)}$ for TM-HEO and TM-MEO(-Co) is -0.26 V versus Na/Na^+ and 0.04 V for TM-MEO(-Mg) and $(Ca_{0.1}Co_{0.225}Ni_{0.225}Cu_{0.225}Zn_{0.225})O$. With our cut-off discharge voltage at 0.01 V, these simple calculations explain why TM-HEO and TM-MEO(-Co) show no electrochemical activity in a Na cell, while TM-MEO(-Mg) and $(Ca_{0.1}Co_{0.225}Ni_{0.225}Cu_{0.225}Zn_{0.225})O$ do, albeit with lower capacities relative to the Li cell. These observations strongly contradict the previous conclusions that the inactivity of TM-HEO in a Na cell is because Na does not form any intermetallic phases with Zn and Mg. We further showed by using TM-MEO(-Mg) that the lower capacity values are due to a partial reaction of this material with sodium. XAS showed that only a fraction of Cu^{2+} in TM-MEO(-Mg) gets reduced to Cu^o, and the remaining elements did not change their oxidation state. This partial reaction has been explained by suggesting that a thick layer of Na_2O formed on the surface of active material particles impedes the transport of Na^+, thus preventing the full sodiation of the oxide particle.

References

1. Guo, S., Liu, C. T. Phase stability in high entropy alloys: formation of solid-solution phase or amorphous phase. *Prog. Nat. Sci. Mater. Int*. **21**, 433-446 (2011).
2. Miracle, D. B. High entropy alloys as a bold step forward in alloy development. *Nat. Commun*. **10**, 1-3 (2019).
3. Gorsse, S., Couzinie, J. P., Miracle, D. B. From high-entropy alloys to complex concentrated alloys. *Comptes Rendus Phys* **19**, 721-736 (2018).
4. Oses, C., Toher, C., Curtarolo, S. High-entropy ceramics. *Nat. Rev. Mater*. **5**, 295-309 (2020).
5. Djenadic, R., Sarkar, A., Clemens, O., Loho, C., Botros, M., Chakravadhanula, V. S. K., Kubel, C., Bhattacharya, S. S., Gandhi, A. S., Hahn, H. Multicomponent equiatomic rare earth oxides. *Mater. Res. Lett*. **5**, 102-109 (2017).
6. Sarkar, A., Wang, Q., Schiele, A., Chellali, M. R., Bhattacharya, S. S., Wang, D., Brezesinski, T., Hahn, H., Velasco, L., Breitung, B. High-entropy oxides: fundamental aspects and electrochemical properties. *Adv. Mater*. **31**, 1806236 (2019).
7. Sarkar, A., Velasco, L., Wang, D., Wang, Q., Talasila, G., de Biasi, L., Kubel, C., Brezesinski, T., Bhattacharya, S. S., Hahn, H., Breitung, B. High entropy oxides for reversible energy storage. *Nat. Commun*. **9**, 3400 (2018).
8. Wright, A. J., Wang, Q., Huang, C., Nieto, A., Chen, R., Luo, J. Form high-entropy ceramics to compositionally-complex ceramics: a case study of fluorite oxides. *J. Eur. Ceram. Soc*. **40**, 2120-2129 (2020).
9. Rost, C. M., Sachet, E., Borman, T., Moballegh, A., Dickey, E. C., Hou, D., Jones, J. L., Curtarolo, S. & Maria, J-P. Entropy-stabilized oxides. *Nat. Commun*. **6**, 8485 (2015).
10. Navrotsky, A., Kleppa, O. J. Thermodynamics of formation of simple spinels. *J. Inorg. Nucl. Chem*. **30**, 479-498 (1968).
11. Navrotsky, A., Kleppa, O. J. Thermodynamics of cation distributions in simple spinels. *J. Inorg. Nucl. Chem*. **29**, 2701-2714 (1967).
12. Navrotsky, A. Thermodynamics of A_3O_4-B_3O_4 spinels solid solutions. *J. Inorg. Nucl. Chem*. **31**, 59-72 (1969).
13. Muller, F., Kleppa, O. J. Thermodynamics of formation of chromite spinels. *J. Inorg. Nucl. Chem*. **35**, 2673-2678 (1973).
14. Hou, S., Su, L., Wang, S., Cui, Y., Cao, J., Min, H., Bao, J., Shen, Y., Zhang, Q., Sun, Z., Zhu, C., Chen, J., Zhang, Q., Xu, F. Unlocking the Origins of Highly Reversible Lithium Storage and Stable Cycling in a Spinel High-Entropy Oxide Anode for Lithium-Ion Batteries. *Adv. Funct. Mater.* **34**, 2307923 (2024).
15. Minouei, H., Tsvetkov, N., Kheradmandfard, M., Han, J., Kim, D.-E., Hong, S. I. Tuning the electrochemical performance of high-entropy oxide nanopowder for anode Li-ion storage via structural tailoring. *Journal of Power Sources* **549**, 232041 (2022).

16. Duan, C., Tian, K., Li, X., Wang, D., Sun, H., Zheng, R., Wang, Z., Liu, Y. New spinel high-entropy oxides $(FeCoNiCrMnXLi)_3O_4$ (X = Cu, Mg, Zn) as the anode material for lithium-ion batteries. *Ceramics International* **47**, 32025–32032 (2021).
17. Marques, O. J. B. J., Walter, M. D., Timofeeva, E. V., Segre, C. U. Effect of Initial Structure on Performance of High-Entropy Oxide Anodes for Li-Ion Batteries. *Batteries* **9**, 115 (2023).
18. Chen, H., Qiu, N., Wu, B., Yang, Z., Sun, S., Wang, Y. A new spinel high-entropy oxide $(Mg_{0.2}Ti_{0.2}Zn_{0.2}Cu_{0.2}Fe_{0.2})_3O_4$ with fast reaction kinetics and excellent stability as an anode material for lithium-ion batteries. *RSC Adv.* **10**, 9736 (2020).
19. Deng, X. L., Zou, K. Y., Momen, R., Cai, P., Chen, J. *et al*. High content anion (S/Se/P) doping assisted by defect engineering with fast charge transfer kinetics for high-performance sodium ion capacitors. *Sci. Bull*. **66**, 1858-1868 (2021).
20. Usiskin, R., Lu, Y. X., Popovic, J., Law, M., Balaya, P. *et al*. Fundamentals, status and promise of sodium-based batteries. *Nat. Rev. Mater*. **6**, 1858-1868 (2021).
21. Guo, Z., Qian, G., Wang, C., Zhang, G., Yin, R. *et al*. Progress in electrode materials for the industrialization of sodium-ion batteries. *Prog. Nat. Sci. Mater*. **33**, 1 (2022).
22. Ghigna, P., Airoldi, L., Fracchia, M. *et al.* Lithiation Mechanism in High-Entropy Oxides as Anode Materials for Li-Ion Batteries: An Operando XAS Study. *ACS Appl. Mater. Interfaces* **12**, 50344-50354 (2020).
23. Bularzik, J., Davies, P. K., Navrotsky, A. Thermodynamics of Solid-Solution Formation in NiO-CuO. *J. Am. Ceram. Soc.* **69**, 453-57 (1986).
24. McCormack, S. J., Navrotsky, A. Thermodynamics of high entropy oxides. *Acta Materialia* **202**, 1-21 (2021).
25. Navrotsky, A. Thermodynamic relations among olivine, spinel, and phenacite structures in silicates and germanates. III. The system $CuOMgOGeO_2$. *J. Solid State Chem.* **11**, 10-16 (1974).
26. Paranthaman, M., David, K. A., Lindemer, T. B. Phase equilibria of the MgO-Cu_2O-CuO system. *Mater. Res. Bull*. **32**, 165-173 (1997).
27. Assal J., Hallstedt, B., Gauckler, L. Thermodynamic evaluation of the Mg-Cu-O system. *Zeitschrift Fur. Met*. **87**, 568-573 (1996).
28. Davydov, A. V., Boettinger, W. J., Kattner, U. R., Anderson, T. J. Thermodynamic Assessment of the Copper-Oxygen System. *J. Phase Equilibria* **15**, 407-410 (1994).
29. Goodenough, J. B. Jahn-Teller phenomena in solids. *Annu. Rev.Mater. Res.* **28**, XVI (1998).
30. Berardan, D., Meena, A. K., Franger, S., Herrero, C., Dragoe, N. Controlled Jahn-Teller distortion in (MgCoNiCuZn)O-based high entropy. *J. Alloys and Comp.* **704**, 693-700 (2017).
31. Diaz-Lopez, M., Chater, P. A., Proux, O., Joly, Y., Hazemann, J.-L., Bordet, P., Pralong, V. Li trapping in nanolayers of cation 'disordered' rock salt cathodes. *J. Mater. Chem. A* **10**, 17415 (2022).
32. Jones, M. A., Reeves, P. J., Seymour, L. D., Cliffe, M. J., Dutton, S. E., Grey, C. P. Short-range ordering in battery electrode, the 'cation-disordered' rock salt $Li_{1.25}Nb_{0.25}Mn_{0.5}O_2$. *Chem. Commun*. **55**, 9027 (2019).

33. King, G., Woodward, P. M. Cation ordering in perovskites. *J. Mater. Chem*. **20**, 5785-5796 (2010).
34. Qiu, N., Chen, H., Yang, Z., Sun, S., Wang, Y. & Cui, Y. A high entropy oxide ($Mg_{0.2}Co_{0.2}Ni_{0.2}Cu_{0.2}Zn_{0.2}$)O with superior lithium storage performance. *Journal of Alloys and Compounds* **777**, 767-774 (2019).
35. Klein, F., Jache, B., Bhide, A., Adelhelm, P. Conversion reactions for sodium-ion batteries. *Phys. Chem. Chem. Phys*. **15**, 15876 (2013).
36. He, K., Lin, F., Zhu, Y., Yu, X., Li, J., Lin, R., Nordlund, D., Weng, T.-C., Richards, R., Yang, X.-Q., Doeff, M. M., Stach, E. A., Mo, Y., Xin, H. L., Su, D. Sodiation Kinetics of Metal Oxide Conversion Electrodes: A Comparative Study with Lithiation. *Nano. Lett.* **15**, 5755-5763 (2015).